The colours of concrete as seen by X-rays and neutrons

Emmanuel Roubin, Edward Ando, Stéphane Roux

The colours of concrete as seen by X-rays and neutrons

Emmanuel Roubin[a,1], Edward Andò[a], Stéphane Roux[b]

[a] *Univ. Grenoble Alpes, CNRS, Grenoble INP1, 3SR, F-38000 Grenoble, France*
[b] *LMT, (ENS Paris-Saclay / CNRS / Univ. Paris-Saclay), 61 avenue du Président Wilson, F-94235 Cachan, France*

Abstract

Both x-ray tomography and neutron tomography give very detailed insight in the microstructure of concrete. However, their different contrasts, due to different compositional sensitivities, make one modality more relevant for some features. The present study shows that both types of images acquired on the same specimen may be registered onto each other, after the statistical joint distribution of absorption coefficients has been learned. A Gaussian mixture model has been used to identify up to five different phases having different signatures. A staggered algorithm consisting in i) adjusting the joint histogram to fit phases and their variances and ii) registering the two 3D images onto each other, within a multi-scale algorithm is presented in details. The analysed experimental data illustrates the benefit of using jointly both modalities as compared to their parallel usage.

Keywords: Concrete microstructure, X-ray computed tomography, Neutron tomography, Digital volume correlation, Multimodal imaging

[1] Author to whom correspondence should be addressed, `emmanuel.roubin@3sr-grenoble.fr`.

1. Introduction

Concrete is a multiphase 3D material. It is now widely recognised that important mechanisms such as failure or fluid percolation reflect this heterogeneity and play out at the meso-scale, where the phases can be identified as aggregates and pores embedded within a mortar matrix. A correct description of the material morphology at this scale is therefore crucial for elucidating these mechanisms. Furthermore, the increasing descriptive power of meso-models *i.e.*, which explicitly take the morphology into account, [1] or morphological models [2] requires the injection of increasingly accurate physical information.

X-ray tomography allows a non destructive access to a 3D field (x-ray attenuation coefficient) at the scale of interest. Due to the large difference in contrast, pores can easily be identified, however, the x-ray attenuation coefficients of aggregates and cement paste are normally very close, making it difficult to distinguish them from each other but not impossible, see [3, 4], as shown in Figure 1, left. Furthermore x-rays are not sensitive to water, a key ingredient of concrete-like materials.

Neutrons interact differently with matter which means that neutron and x-ray attenuation coefficients can be very different for the same material. A striking example is that neutrons are sensitive to water which allows both of the x-ray's limitations to be tackled — however with a limitation on the spatial resolution. The presence and movement of water (of more generally fluids) within concrete is of major interest for the mechanical behaviour of concrete under high stresses [5, 6, 7], for speed of chemical degradation [8], for resistance to fire [9] as well as for its quality as a material for containment [10, 11]. A number of studies have been carried out on concrete using neutron radiography, allowing water infiltration to be measured with ease. In the context of tomography on concrete, the sensitivity to water leads to a different field for the phase description, as shown in Figure 1, right. Ref. [12] presents an excellent example of the interest of neutron tomography for concrete, where the loss of water during a simulated fire can easily be quantified. Furthermore, the *isotope*

sensitivity of neutrons allows flow paths to be measured in saturated conditions such as in Ref. [13], which incidentally is the source of the data that will be studied herein.

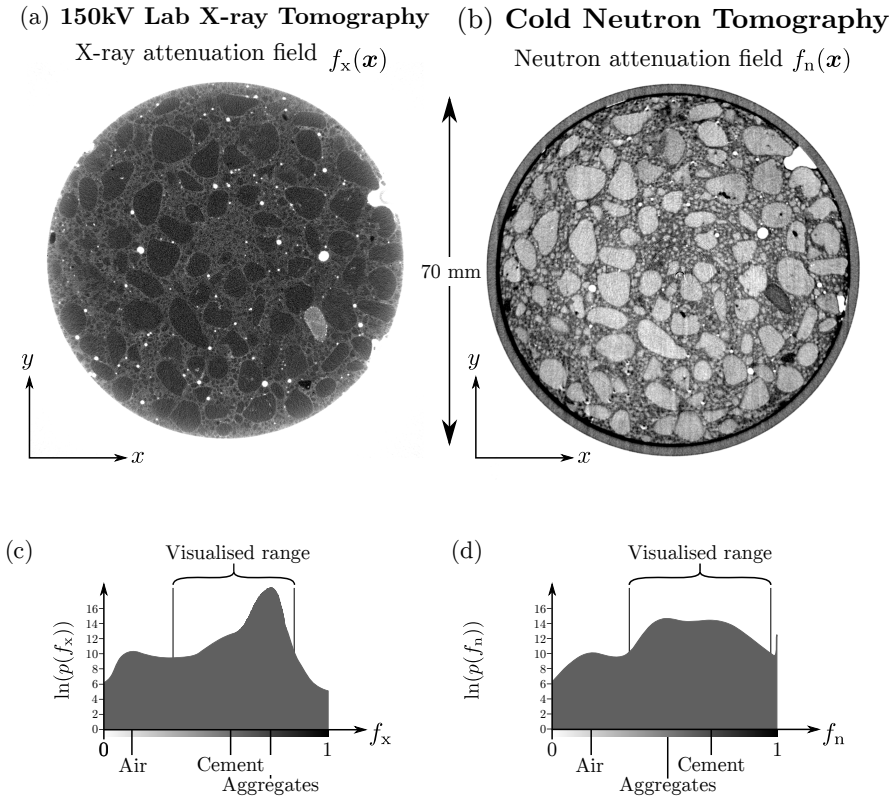

Figure 1: Figure adapted from [13].The top row presents the similar horizontal slices of the sample studied coming from reconstruction of x-ray (a) and neutron (b) tomographies. Please note that for compatibility with a white background in print, the colour map has been inverted compared to the conventional for reconstructed volumes, such that low attenuation is white and high attenuation is black. Furthermore attenuation values for both fields have been scaled and offset to fit in the [0, 1] range. The field of x-ray attenuation is called f_x and the neutrons f_n. They are both defined over a Cartesian coordinate system $\boldsymbol{x}$. The bottom row (c) and (d) presents the corresponding natural logarithm histogram $\ln(p)$ of the two fields calculated inside the specimen.

The authors believe that the combination of x-ray and neutron tomography provides an extremely valuable tool for the study of numerous meso-scale

mechanisms in concrete. In fact, in recent years, a number of neutron centres offer coupled x-ray and neutron tomography [14, 15, 16, 17], providing complementary fields of attenuation. A better description of the phases of concrete can thus be obtained by combining both fields on the condition that they are spatially commensurable (*i.e.*, with a common coordinate system). Indeed, due to a number of uncontrollable variables (mechanical noise, small variations in the source, *etc.*) after separate reconstruction, the two resulting fields will not be perfectly aligned. One might think that alignment by eye using recognisable morphological features (such as the top right external pore in Figure 1) would yield sufficient well aligned image, but experience shows that, even with a rigid body motion constraint, 3D rotations are very hard to gauge. A change of pixel size between the two images leads to even more complex transformations (non rigid-body motion) that render alignment even more difficult.

This article presents the technical details of the algorithm proposed in [18] and applies it to neutron and x-ray tomographies of concrete (those shown in Figure 1). This yields a registered neutron image that matches the x-ray image with subpixel accuracy. This procedure can be seen as a generalisation of a classical DVC registration [19] to fields obtained with multiple modes of acquisition (*i.e.*, multimodal registration). The final result is therefore a 3 dimensional vector-valued "image" containing two attenuation coefficients. In this paper, we use the "Gaussian Mixture" representation of the different phases which, as a bonus, naturally provides an identification of the phases [20].

2. X-ray and neutron image of concrete

2.1. Description of data

Figure 1 shows two horizontal slices from tomographies of the same sample — which has been prepared with heavy water (D_2O) to facilitate neutron penetration.

The x-ray attenuation field — which is closely related to material density — presents three different phases. Voids (filled with air or D_2O) have a very

different value (white) from that of the solid phase and are thus easily identifiable. The aggregate and the mortar matrix can easily be distinguished by eye, more because of their texture than due to contrast since the values (black) are very close. The neutron attenuation field — which does not track density — has different contrast between the phases which clearly discriminates the aggregates from the matrix. The spatial disposition of the aggregates in both images is in rough agreement since they have been aligned by eye.

In the following, the value of the x-ray attenuation field at 3D spatial position $\boldsymbol{x} = (x, y, z)^\top$ is noted $f_\mathrm{x}(\boldsymbol{x})$ (f_x for short). The neutron attenuation field is referred to as f_n. It is important to note that in this case, these fields come from the reconstruction of attenuation measurements made with polychromatic beams meaning that the resulting field represents a frequency-lumped attenuation coefficient which introduces a certain degree of arbitrariness in the field. In the grey level fitting that follows, beam hardening is likely to have a strong adverse effect. Both fields are normalised so that they take values in $[0, 1]$. For convenience, vector notation referring to the same spatial position in both x-ray and neutron attenuation fields $\boldsymbol{\varphi} = (f_\mathrm{x}, f_\mathrm{n})^\top$ is used.

For each image, a histogram of grey levels can be computed showing the probability distribution p of grey levels — distribution of $p(f_\mathrm{x})$ or $p(f_\mathrm{n})$ inside the Region Of Interest (ROI) — corresponding to attenuation fields. In Figure 1, the two histograms show peaks corresponding to the phases mentioned above. A very rough approximation of the mean values of the attenuation fields for each phase can be obtained by taking an average over a small area wholly within the phase (see Table 1).

2.2. Joint histogram

Since both images have the same format and have been put roughly in coincidence, a joint histogram of $p(\boldsymbol{\varphi})$ can therefore be computed over the ROI collecting the f_x and f_n values at the same pixel location. Both grey levels are discretised into a number n_bins of grey level intervals (called bins), so that p is discretised to a $n_\mathrm{bins} \times n_\mathrm{bins}$ matrix denoted $[p]$.

Table 1: Approximate mean values μ_x and μ_n of f_x and f_n for the three main phases identified. It is important to note that these values have been offset and rescaled, and are therefore expressed in arbitrary units.

	X-ray attenuation (μ_x)	Neutron attenuation (μ_n)
Aggregates	0.77	0.48
Voids	0.12	0.18
Mortar	0.72	0.68

Applied to the images above, and taking the inside of the specimen as ROI, the two-dimensional joint histogram $[p]$ is shown in Figure 2. Because registering the circular cross section is easily done, and as is apparent in Figure 1, the main source of misalignment appears to be a rotation whose axis is normal to the plane of the slices presented. Given both the size and the volume fraction of the aggregates in the material, even for this relatively severe misalignment, some $\boldsymbol{x}$ point to aggregates in both images or mortar in both images. This leads to two high spots in Figure 2 (left) that represent the $\boldsymbol{\varphi} = (f_x, f_n)^\top$ couplets for aggregates and for the mortar matrix, at approximately the values in Table 1. However, due to misalignment, many $\boldsymbol{x}$ will point to different phases, which spreads out the peaks. A clear example is the absence of a peak for voids, which, due to their small sizes almost never share a common $\boldsymbol{x}$. Indeed, the zone around $f_x \approx 0.1$ and $f_n \in [0.45, 0.8]$ corresponds to voids in the x-ray intersecting with solids in the neutron image. Similarly, the zone around $f_n \approx 0.2$ and $f_x \approx 0.7$ corresponds to voids in the neutrons intersecting with the (similarly-valued) solids in the x-ray image. The absence of peak for $f_x \approx 0.1$ and $f_n \approx 0.2$ is simply the result of a misalignment of the two images.

An approximate (estimated by eye) initial guess of a $-15°$ rotation is applied to the f_n field to increase spatial coherence, yielding the joint histogram in Figure 2 (right). The intensity of the peaks for aggregates and mortar are not significantly improved, but the appearance of a peak corresponding to voids is

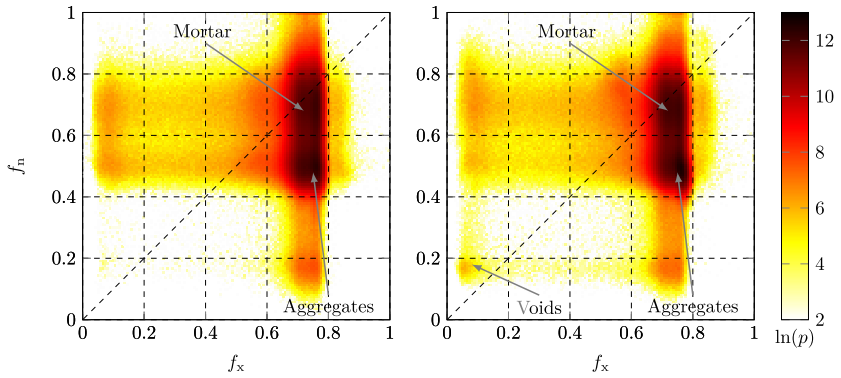

(a) Without initial guess (b) With initial guess

Figure 2: Joint histogram of the two normalised 3D fields presented in Figure 1 which has been computed considering the inside of the specimen as the ROI

a sign of better alignment (a misalignment smaller than the size of the biggest voids).

The lack of separation between the mortar and aggregate peaks is probably due to fact that the sand particles embedded in the mortar are not yet well aligned, due to their small size. It is of clear interest to be able to quantify the similarity between two images. Equation (15) in [18] presents a way in which this can be quantified by a scalar $\mathcal{L}$ (referred to as likelihood) defined (when correlation is ignored) by

$$\mathcal{L} \propto \prod_{\boldsymbol{x} \in \mathrm{ROI}} p(\boldsymbol{\varphi}(\boldsymbol{x})) \tag{1}$$

In practice, the discrete version of p, *i.e.*, the binned joint histogram, $[p]$, is used to compute $\mathcal{L}$. The logarithm of this quantity [Equation (16) in Ref. 18] "assumes a convenient form" in that it turns the product into a simple sum

$$\ln(\mathcal{L}) = \sum_{\boldsymbol{x} \in \mathrm{ROI}} \ln\left(p(\boldsymbol{\varphi}(\boldsymbol{x}))\right) + \text{constant} \tag{2}$$

Incidentally, this explains the choice of the logarithm of counts in the joint histogram plotted in Figure 2. Applied to the left image (with constant = 0) this yields a value of approximately 33600 (arb. units) where with the initial guess of $-15°$ this improves to approximately 34900 (arb. units).

At this point, let us emphasise a subtlety: p is known only when the two images are exactly registered. Otherwise, the joint histogram being approximative, the likelihood is erroneous. However, because of the spatial correlations in the real microstructure, the error in $\mathcal{L}$ is limited, and it will be shown in the following section 3, that even using an imperfect likelihood, one may better register images and thus gain access to a more accurate joint distribution, and hence a better $\mathcal{L}$.

2.3. Fitting the joint histogram

With the objective of obtaining a better alignment between the two images, an image correlation method will be developed in the next section. Regular image correlation cannot be applied directly in this context due to the inconsistency of the values of the fields f_{x} and f_{n}. Fitting the relevant peaks of the joint histogram will allow any pair of values $\boldsymbol{\varphi} = (f_{\mathrm{x}}, f_{\mathrm{n}})^{\top}$ to be assigned to a given fitted peak and therefore a phase.

Let us consider N_{phase} phases, each characterised by a bivariate Gaussian distribution, $p_i(\boldsymbol{\varphi})$ for phase i, where bivariate refers to the two 3D measurements of their absorption coefficient for x-rays and neutrons, gathered into a vector $\boldsymbol{\varphi} = (f_{\mathrm{x}}, f_{\mathrm{n}})^{\top}$. In other words, p_i represents the probability distribution of possible pairs of grey values knowing that, at this specific point, the material phase is i. As a probability distribution, its sum over all possible $\boldsymbol{\varphi}$ is 1. Each phase i has a corresponding mean vector $\boldsymbol{\mu}_i = (\mu_{\mathrm{x}}, \mu_{\mathrm{n}})^{\top}$, and covariance matrix $\mathbf{C}_i$ such that the probability distribution for $\boldsymbol{\varphi}$ within this phase i is

$$p_i(\boldsymbol{\varphi}) = \frac{1}{2\pi \det(\mathbf{C}_i)} \exp\left(-(1/2)(\boldsymbol{\varphi} - \boldsymbol{\mu}_i)^{\top}(\mathbf{C}_i)^{-1}(\boldsymbol{\varphi} - \boldsymbol{\mu}_i)\right) \tag{3}$$

The i individual probability maps for each phase can be combined in order to give the probability of measuring a given $\boldsymbol{\varphi}$. In order to do this, the probability maps for each phase need to be weighted, and this is done by the relative quantities in the material being studied, *i.e.*, the weights to use are naturally the volume fractions of each phase. Introducing q_i the volume fraction of phase

i, the probability to measure a specific $\boldsymbol{\varphi}$, is therefore

$$p(\boldsymbol{\varphi}) = \sum_{i=1}^{N_{\text{phase}}} q_i p_i(\boldsymbol{\varphi}), \tag{4}$$

whose sum is again 1 over all possible $\boldsymbol{\varphi}$, due to the weighting by each phases' volume fraction q_i. Although volume fractions are an initial microstructural measurement of interest, without an initial segmentation these cannot be obtained accurately, but they can be computed from the fitting of each phase. With ϕ_i as the height of the peak in $p(\boldsymbol{\varphi})$ for each phase i

$$q_i \equiv \phi_i 2\pi \det(\mathbf{C}_i) \tag{5}$$

The inverse covariance matrix for each Gaussian distribution is parametrised by

$$(\mathbf{C}_i)^{-1} = \begin{pmatrix} a_i & b_i \\ b_i & c_i \end{pmatrix} \tag{6}$$

Thus, each phase requires four parameters (ϕ_i, a_i, b_i, c_i) to be defined.

The presence of Gaussian distributions in the joint histogram can have different origins:

- *Uncorrelated* Gaussian noise in each measurement of uniform x-ray and neutron attenuation fields (implying in that case $b_i = 0$).
- A real Gaussian distribution of x-ray and neutron attenuation fields due to some properties of the material phases (such as a compositional randomness at a lower scale than resolved with the voxels).

However, even if there is no justification from basic principles that the distribution should assume a Gaussian mixture form, it should also be noted that if enough phases are taken into account, such a description is not restrictive. Moreover, this assumption is very convenient mathematically (see appendix).

The fit is performed on the discrete (binned) joint histogram $[p]$, the position $(\mu_{\text{x}}, \mu_{\text{n}})$ and value ϕ of the peaks come from a maxima finder, leaving just $\mathbf{C}_i$ (or a_i, b_i and c_i) as free variables (see Algorithm 1). Setting a minimum

distance between fitted peaks is a good way of avoiding spurious peaks in $[p]$. Furthermore, a convenient sanity check for the fitted peaks is the positiveness of the matrix $\mathbf{C}_i$ (meaning that both determinant and trace should be positive, or equivalently that the two eigenvalues of $\mathbf{C}_i$ are positive) which indicates that the fitted Gaussian represents indeed a maximum.

Algorithm 1 Gaussian fitting

```
Compute joint histogram
Select number of phases N_phases
for k in [1..N_phases] do
    Find the position of the highest maxima μ_i
    Select a neighbourhood of μ_i
    Fit the joint histogram in this neighbourhood as a second-order polynomial
    Sanity check that the polynomial has a positive curvature tensor
    Subtract off the fitted Gaussian from the joint distribution
    (or cut-out region based on the probability value q_i p_i)
end for
```

In this particular case, only two peaks are selected for fitting since despite the appearance of a (void, void) peak, the third highest peak is still due to a misalignment of voids. Table 2 gives the values found by the Gaussian fit for the histogram shown in Figure 2 (right), and Figure 3(a) shows the result of the Gaussian fit of these two peaks.

It can be noted from Table 2, that since b is small compared to a and c, it can be deduced that the correlation between x-ray and neutron attenuation fields is also small. This is particularly the case for the mortar which is consistent with an uncorrelated random noise as being at the origin of a Gaussian distribution. This may be less true for the aggregates indicating some minor correlation between the two attenuation coefficients. In any case, imposing $b = 0$ in the correlation matrix in the algorithm for both distributions neither improves nor degrades the quality of the registration.

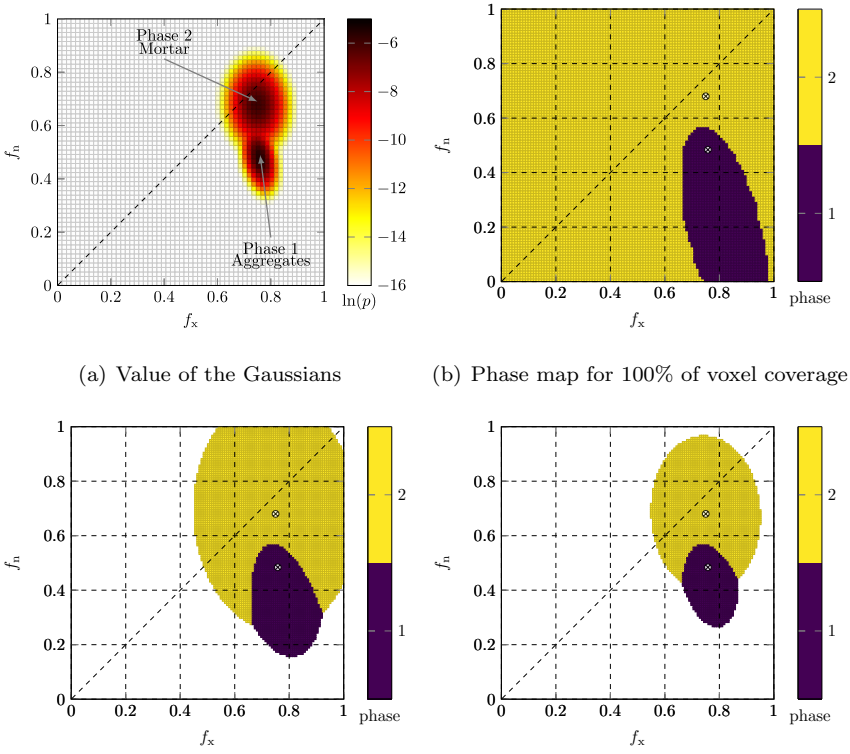

(a) Value of the Gaussians

(b) Phase map for 100% of voxel coverage

(c) Phase map for 99% of voxel coverage

(d) Phase map for 98% of voxel coverage

Figure 3: (a): Fit of the joint histogram with two Gaussians corresponding to aggregates and mortar (see Figure 2, right). The value shown for each f_x and f_n is the maximum of both fits. (b-d): phase map for different voxel coverage.

2.4. Phase identification

It is reminded here that every (q_i weighted) Gaussian in $[p]$ represents a material phase. Given at least two well-fitted Gaussians, it is of primary importance to our objective to estimate the probability $\pi_i(\boldsymbol{\varphi})$ that a pair of greylevels $\boldsymbol{\varphi}$ belongs to phase i, allowing for classification.

Bayes' rule leads to

$$\pi_i(\boldsymbol{\varphi}) = \frac{q_i p_i(\boldsymbol{\varphi})}{\sum_{j=1}^{N_{\text{phases}}} q_j p_j(\boldsymbol{\varphi})} \tag{7}$$

so that the most likely phase is simply the one that maximises $q_i p_i(\boldsymbol{\varphi})$ among all phases i. Thus, in the coordinate system of the joint histogram $\boldsymbol{\varphi}$, a phase

Table 2: Table of parameters for Gaussian fit of the joint histogram in Figure 2 (right) to be compared to the approximate values in Table 1

Fit Value	Phase 1 (Aggregates)	Phase 2 (Mortar)
ϕ (q)	0.046 (0.304)	0.025 (0.404)
μ_{x}	0.76	0.75
μ_{n}	0.48	0.68
a	3154.2	901.0
b	495.9	25.0
c	835.9	441.4

map $\gamma(\boldsymbol{\varphi})$ can be established by "labelling" each combination of greyvalues of $\boldsymbol{\varphi}$ with the most likely phase i:

$$\gamma(\boldsymbol{\varphi}) = \underset{i}{\mathrm{Argmax}}[\pi_i(\boldsymbol{\varphi})] = \underset{i}{\mathrm{Argmax}}[q_i p_i(\boldsymbol{\varphi})] \tag{8}$$

The phase map deduced from Figure 3(a) can be seen in Figure 3(b), for all combinations of $\boldsymbol{\varphi}$. It can be observed that every grey level pair is associated to a phase, even those far from a peak. This can be improved by selecting a more appropriate number of phases being fitted, which in turns requires a better alignment of the images.

For safety, $\boldsymbol{\varphi}$ pairs in $\gamma(\boldsymbol{\varphi})$ that are far from fitted peaks can be excluded — *i.e.*, assigned a "non-phase". A threshold on the minimum *Mahalanobis distance* [21] of each greyscale pair to the each Gaussian fit is made, rather than a cut-off on the probability level. This is justified by the fact that excluding $\boldsymbol{\varphi}$ values requires the identification of unrealistic greyvalues, which should not depend on the quantity of the detected phase. More pragmatically, it has been found that in the presence of phases with small volume fractions (such as the voids in this case) reasonable probability cut-offs for the more probable phases coincide with the peak for the voids, and thus completely erase them. This threshold, applied to the fit of a bivariate Gaussian distribution, represents a cut-off value

based on the distance from the mean (the equivalent to a standard deviation cutoff in 1D), and is independent of the fitted height. A useful metric for the evaluation of the impact of this threshold is the quantification of the number of retained voxel pairs (*i.e.*, in this case being in phase 1 or 2) that we call "voxel coverage". Figures 3(c-d) represent two different thresholds that yield a 99% and 98% voxel coverage.

Finally, a useful output of the fitting is the ability to obtain the spatial distribution of the phases within the scanned specimen. This can be computed by using the phase map to classify the phase of all the voxels in space $\gamma(\boldsymbol{x}) = \gamma(\boldsymbol{\varphi}(\boldsymbol{x}))$.

The fitting of the phases therefore yields a *mapping* of the correspondences of grey levels between modalities. This information is essential to allow the alignment of the images to be pursued with a DVC-based image registration technique adapted to multimodality that will be presented in the next section and applied to the test case in the section after.

3. Multimodal registration

The multimodal registration algorithm in [18] is essentially an extension of classical Digital Image Correlation methods, whose aim is to determine the linear transformation operator $\boldsymbol{F}$ (not to be confused with the greyvalue field f_{x}) affecting the coordinates of one modality image, say f_{n}, so that it matches the reference one, f_{x}. In order to account for noise and other sources of imperfection, a variational formulation is proposed through the minimisation of the functional $\mathcal{T}$

$$\mathcal{T}(\boldsymbol{F}) = \sum_{\boldsymbol{x}\in\mathrm{ROI}} \Phi^2(f_{\mathrm{x}}(\boldsymbol{x}), f_{\mathrm{n}}(\boldsymbol{F}\cdot\boldsymbol{x})) \tag{9}$$

representative of the quality of the match between the two images. To this end, Equation 2 provides the necessary ingredients based on the joint histogram, yielding the following definition (with a negation to ensure the function is at a minimum at the best match)

$$\Phi^2(\boldsymbol{\varphi}) = -\ln(p(\boldsymbol{\varphi})) \tag{10}$$

In Equation 4, p was proposed to be approximated by the sum of a few Gaussian distributions, thus finally giving a Φ^2 potential of the form

$$\begin{aligned} \Phi^2(\boldsymbol{\varphi}) &= -\ln\left(\textstyle\sum_i \phi_i \exp(-(1/2)(\boldsymbol{\varphi}-\boldsymbol{\mu}_i)^\top(\mathbf{C}_i)^{-1}(\boldsymbol{\varphi}-\boldsymbol{\mu}_i))\right) \\ &\approx (1/2)\min_i\left[(\boldsymbol{\varphi}-\boldsymbol{\mu}_i)^\top(\mathbf{C}_i)^{-1}(\boldsymbol{\varphi}-\boldsymbol{\mu}_i)) - \ln(\phi_i)\right] \end{aligned} \tag{11}$$

where i accounts for all the fitted peaks and the minimum depends on the values of $\boldsymbol{\varphi} = (f_\mathrm{x}, f_\mathrm{n})$.

The registration algorithm itself is presented in [18, equations 5 to 14] and developed in more detail in the appendix of this paper.

In the interests of robustness and speed, we start the registration on highly downscaled images which allows high frequency variations to be erased and guarantees the applicability of the Taylor expansion in the case of large displacements. Registrations are repeated on progressively more detailed images, using previously obtained transformation as initial conditions ["multiscale" approach in 18].

Images are thus low-pass filtered, and because the high frequency information has been (temporarily) erased, it is no longer necessary to sample the image pixel per pixel. Thus if a filter of size 2 pixels in each space dimension is used, then the image can be downsampled by a factor $2^3 = 8$, allowing faster and less memory demanding data manipulation. Different types of filters may be used, the easiest of which is known as "binning". "N-binning" means $N \times N \times N$ voxels are averaged together. 1-binning therefore is the original image (no downscaling), 2-binning halves the number of voxels in each direction, 4-binning divides by 4 the number of voxels in each direction, *etc.* Usually bin levels are chosen as a geometric series as 2^I values through a recursive procedure. Once "2^i-binned" images are registered, higher frequencies can be restored and registration can be performed more accurately while the largest displacements are already accounted for. The final step of the registration is performed with the original images, thus without loss of information, and yet benefiting from the robustness offered by the coarsest resolution. Alternatively a Gaussian filtering followed by down sampling can be used following a classical Gaussian multiscale pyramidal

approach. It has been found unnecessary here.

A further advantage of the multiscale pyramidal approach is that noise is depressed as higher and higher degrees are considered. In the images shown, 4-binning or even 8-binning can be applied without loosing the coarse texture provided by the cement paste and the aggregates. See [18] Algorithm 1 for details.

4. Application to concrete

4.1. Initial registration

The ROI is defined as a crop of the data presented in figure 1 to avoid the textureless background outside the specimen. This crop yields a 400^3 voxel volume at full-scale (1-binning).

The data is first downscaled to 4-binning (*i.e.*, a 100^3 voxel volume). To start with, the joint histogram $[p]$ shown on the top left of Figure 4 is computed by applying the initial guess of $-15°$ to f_n. It is important to note the difference with the histogram presented in Figure 2 (right) which also takes into account the initial guess but at a different binning level. The applied binning has two effects: it denoises the data — giving sharper peaks — and erases the small features such as pores — peak missing at $(f_\mathrm{x}, f_\mathrm{n}) \approx (0.1, 0.2)$ for example. From this histogram two maxima are identified (marked by white crosses) and two Gaussian ellipsoids are fitted. Using these fits the phase diagram is computed with a target voxel coverage of 99%. Avoiding pairs of values far from peaks appears to allow slightly faster convergence of the registration. The two main phases appeared clearly (in order of descending peak value): the mortar matrix and the aggregates.

Over the iterations $\boldsymbol{F}$ is updated and from it, translation and rotation are extracted. The convergence condition is set to be $\|\delta\boldsymbol{F}\| < 5.10^{-4}$ and 27 iterations are needed to reach convergence at the 4-binning level. Figure 5 shows the evolution of both rotation and translation and Table 3 the value at convergence (for all scales).

After convergence at this binning level, the $\boldsymbol{F}$ operator is rescaled (translation part multiplied by 2) and used as an initial guess for 2-binning level (*i.e.*, a 200^3 voxel volume). As before, the joint histogram is computed by applying this initial guess to f_n. As shown in Figure 4, the guess is sufficiently good and the scale is sufficiently fine to see a new peak corresponding to the pores. This new phase is added to the list of phases to be fitted by Gaussian ellipsoids which results in a 3 phases diagram: 1 being the aggregates, 2 the mortar matrix and 3 the pores. The registration is continued at this binning level, converging after 11 iterations to the values shown in Table 3.

As above, the previous converged $\boldsymbol{F}$ is used as an initial guess for 1-binning level (*i.e.*, a 400^3 voxel volume). A new joint histogram is computed and the same 3 peaks are fitted leading to the values shown in Table 3 after 16 iterations.

The difference between the joint histograms for 2-binning and 1-binning is not mainly due to the change in $\boldsymbol{F}$ (which is small) but rather to a combination of both decreasing partial volume effects and increasing spatial resolution.

Figure 5 reveals the significant interest in performing binning where the majority of the registration is performed at the lowest binning level and therefore at high speed. However, the downscaled registrations seem to converge to a different solution than the higher scale. This is especially true for the z component of the translation.

The registration run directly on the original images without downscaling approach converges after 212 computationally expensive iterations (to be compared to a total of 57 iterations with the multiscale approach), to a transformation which is close to that obtained with the downscaling approach (*i.e.*, within 0.05 pixels displacement and 0.005°).

In order to visually check the commensurability of the registered fields, checkerboard patterns mixing the two fields f_x and f_n are presented in Figure 6 on the full image (including the background). On the top left, the initial guess of -15° shows the lack of similarity between the two fields. On the top right, the result of first registration at this binning level already shows a good correspondence, as seen above. On the next two checkerboards at finer resolu-

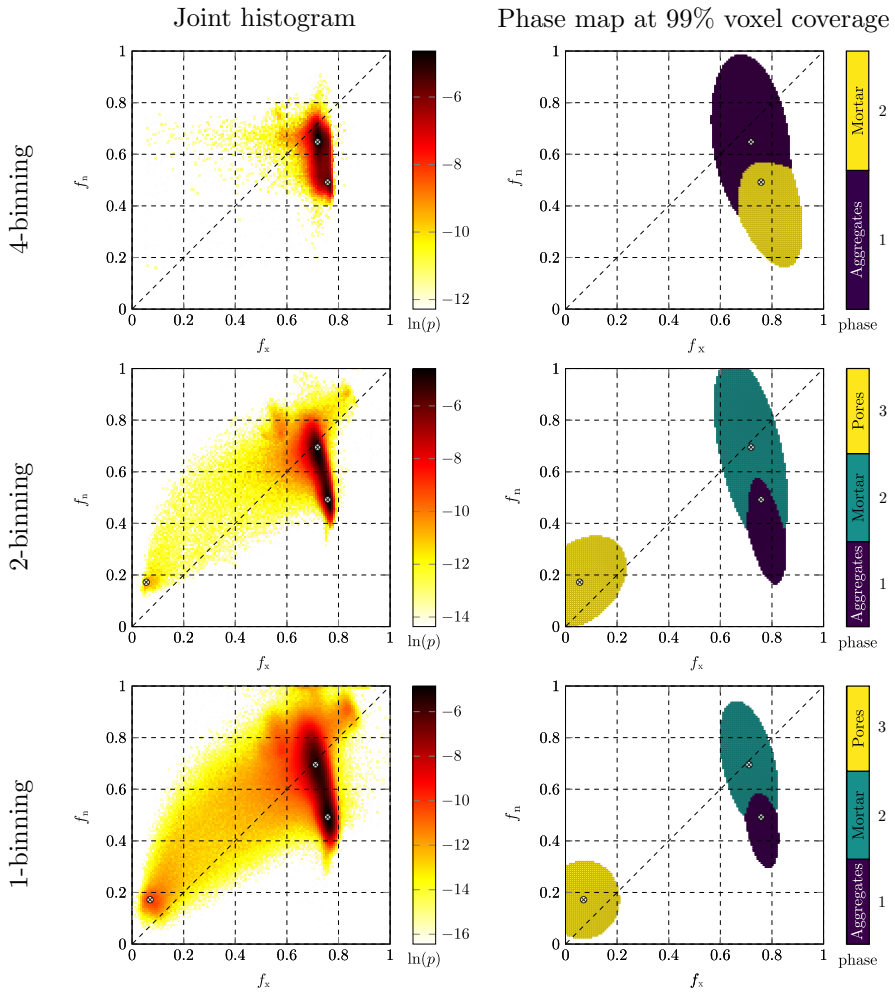

Figure 4: Joint histograms (left) and phase maps (right) before entering registration algorithm for each binning level

tions, the continuity of the phases is visually satisfactory.

4.2. Final phase identification at full-scale

To identify the phases present in this material, the final transformation obtained above at the binning 1 scale with three phases is used as an initial guess for another run of the registration approach with an increased number of phases. This run is expected to converge quickly. In this case, 5 phases are selected with

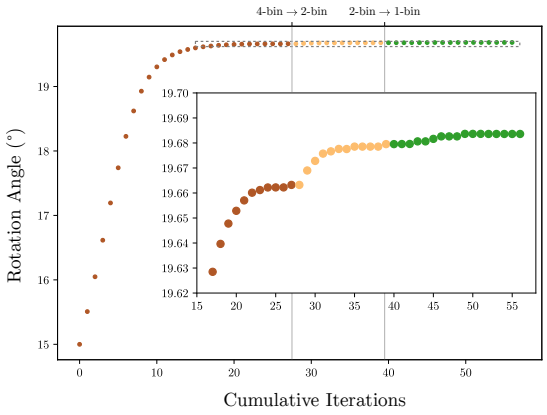

(a) Rotation angle

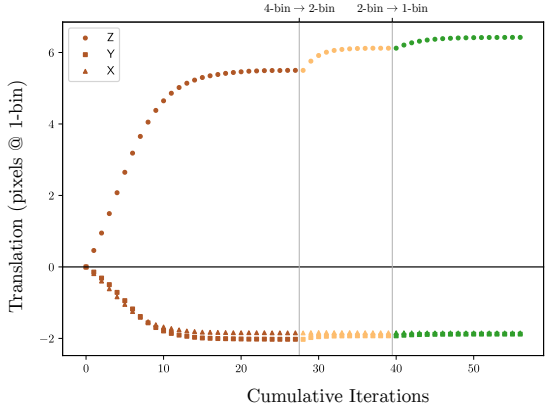

(b) Translation

Figure 5: Rotation angle (top) and translation (bottom) over the cumulative iterations of the registration over the three binning level. Translation of binning 4 and 2 are scaled to binning 1 voxel size (*i.e.*, multiplied by 4 and 2, respectively). The inset of (a) is a magnified view of the data contained in the dotted box.

99% coverage, as shown in Figure 7 (left). This yields the phase identification presented in Figure 7 (right).

The aggregate and mortar phase are easily identified as phases 1 and 2, respectively. Phase 3 corresponds to a mineralogically different aggregate (it can be observed in Figure 1, bottom right of the slice, as having a lower X-ray attenuation and higher neutron attenuation). This phase occupies a rather

Table 3: Converged translation and rotation values at each binning level for axes (x, y, z). The rotations are expressed as a rotation vector in the axis and angle format.

Binning level	Translation [pixels @ Bin 1]	Rotation [deg]	Iterations
4	$-2.03, -1.85, 5.50$	$-0.59, 0.11, -19.65$	27
2	$-1.93, -1.84, 6.12$	$-0.58, 0.07, -19.67$	11
1	$-1.88, -1.85, 6.42$	$-0.58, 0.07, -19.68$	16

large area in the phase diagram. This may be due to the region over which the Gaussian peak is fitted, as unfortunately, partial volume voxels between mortar matrix and pores often fall into this zone. This explains the nonphysical presence of this phase around pores. The centre of large pores are well identified as phase 4. However, it can be observed that the non phase (in white) usually is in the vicinity of pores. Indeed, in addition to partial volume effects, artefacts affect the reconstruction of these low attenuations more than the other phases. Phase 5 corresponds to small, highly attenuating inclusions scattered all over the specimen, which may be metallic in origin.

On the whole, the meso-scale morphology of concrete can be very accurately classified thanks to the registration procedure. Let us stress that with one single modality, it would have been impossible to identify those phases which have a significant overlap with other ones in a single modality histogram.

5. Conclusions

This paper presents the technical details of an algorithm to researchers in the field of concrete and cement research, an essential component of the groundbreaking new measurement that combined neutron and x-ray tomography represents. The ability to register neutron and x-ray fields, as well as to obtain an identification of phases, allows a number of cutting-edge research questions to be answered — for example regarding complex hydro-mechanical phenomena in

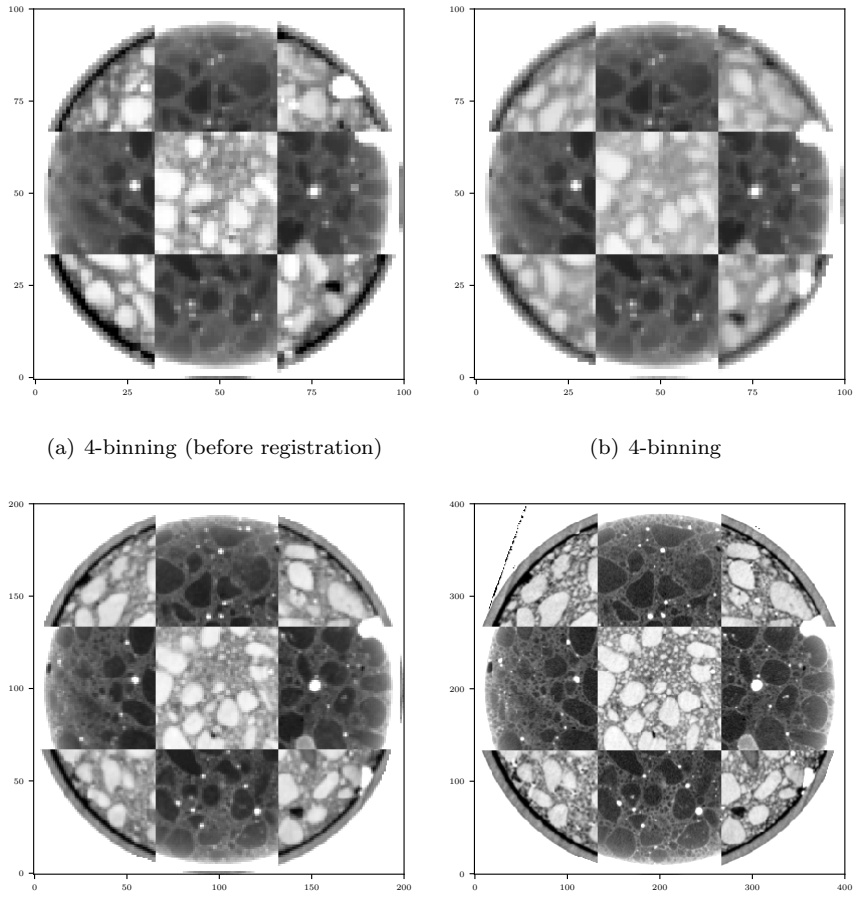

(a) 4-binning (before registration)

(b) 4-binning

(c) 2-binning

(d) 1-binning

Figure 6: Checkerboard pattern of f_{x} (dark) and f_{n} (light) as per Figure 1

concrete.

The algorithm as presented here is implemented in the Spam toolkit, an open-source image analysis toolkit [22] where an example on another set of concrete images is presented. This form of release is expected to ease and maximise its use.

Furthermore, the technique presented here, which is ideally suited to research on concrete, also presents some interest for materials, where the coupling of neutron and x-ray tomography is beneficial. Registrations have been successful

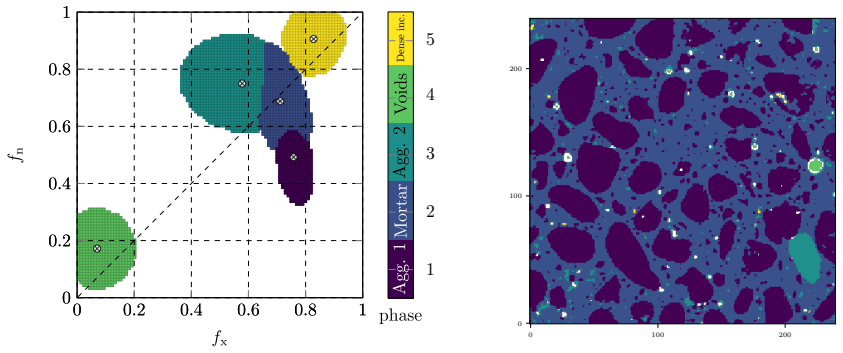

(a) (b)

Figure 7: (a): Phase map $\gamma(\boldsymbol{\varphi})$ with 99% coverage after final registration (b): and corresponding identification of the phases $\gamma(x)$ within the ROI (right). The pixels in white correspond to the 1% of pixels in the non-phase. Phases, from bottom to top on the colour bar: Most numerous aggregate type, Mortar matrix, Second aggregate type, Voids, and, Dense inclusions (negligible volume fraction – possibly metallic)

on rocks (in the initial presentation of the technique [18]), bones with metallic implants, roots growing in a moist granular material, and asphalt (all of these a recent results soon to be published).

6. Perspectives

A number of further paths of development stem from this work. The phase allocation for partial volume voxels could certainly be improved, providing a better assignment to uncertain voxels. At a more ambitious level, it would be extremely desirable to incorporate spatial correlations in the analysis, with neighbouring pixel analysis.

A path further in the future for advanced experiments on concrete is the development of a combined image correlation minimisation, taking into account two fields. In the case where a neutron and x-ray scans of a reference state, and subsequent scans of a deformed state have been acquired (and after due application of the algorithm discussed herein) a measurement of the kinematics that map one phase into the next would be extremely valuable to exploit the

highly complementary information provided. It may also offer new opportunities, such as speeding up neutron tomography, which would imply to deal with a higher amount of noise.However, because x-ray tomography would be performed simultaneously, a prior guess of "neutron contrast" image can be proposed to a neutron tomographic reconstruction algorithm leading to a much more robust and noise-tolerant tool. In a similar spirit, these two modalities can also be used with different spatial resolution, allowing the finer one to inform the coarser one.

References

[1] E. Roubin, A. Vallade, N. Benkemoun, J.-B. Colliat, Multi-scale failure of heterogeneous materials: A double kinematics enhancement for embedded finite element method, International Journal of Solids and Structures 52 (2015) 180 – 196. doi:https://doi.org/10.1016/j.ijsolstr.2014.10.001.
URL http://www.sciencedirect.com/science/article/pii/S0020768314003710

[2] E. Roubin, J.-B. Colliat, N. Benkemoun, Meso-scale modeling of concrete: A morphological description based on excursion sets of random fields, Computational Materials Science 102 (2015) 183 – 195. doi:https://doi.org/10.1016/j.commatsci.2015.02.039.
URL http://www.sciencedirect.com/science/article/pii/S0927025615001408

[3] P. Trtik, P. Stähli, E. Landis, M. Stampanoni, J. Van Mier, Microtensile testing and 3d imaging of hydrated portland cement, in: Proceedings 6th international conference on fracture mechanics of concrete and concrete structures (FraMCoS-VI). London: Taylor & Francis, 2007, pp. 1277–1282.

[4] O. Stamati, E. Roubin, E. Andò, Y. Malecot, Phase segmentation of concrete x-ray tomographic images at meso-scale: Validation with neutron tomography, Cement and Concrete Composites 88 (2018) 8 – 16. doi:https://doi.org/10.1016/j.cemconcomp.2017.12.011.
URL http://www.sciencedirect.com/science/article/pii/S095894651730642X

[5] T. Gabet, Y. Malécot, L. Daudeville, Triaxial behaviour of concrete under high stresses: Influence of the loading path on compaction and limit states, Cement and Concrete Research 38 (3) (2008) 403–412.

[6] X.-D. Vu, M. Briffaut, Y. Malecot, L. Daudeville, B. Ciree, Influence of the

saturation ratio on concrete behavior under triaxial compressive loading, Science and Technology of Nuclear Installations 2015.

[7] Y. Malecot, L. Zingg, M. Briffaut, J. Baroth, Influence of free water on concrete triaxial behavior: the effect of porosity, Cement and concrete researchSubmitted.

[8] V. G. Papadakis, C. G. Vayenas, M. N. Fardis, Physical and chemical characteristics affecting the durability of concrete, Materials Journal 88 (2) (1991) 186–196.

[9] T. Harmathy, Effect of moisture on the fire endurance of building elements, in: Moisture in materials in relation to fire tests, ASTM International, 1965.

[10] P. Mivelaz, Etanchéité des structures en béton armé: fuites au travers d'un élément fissuré, Ph.D. thesis, Thèse Ecole Polytechnique Fédérale de Lausanne. Suisse (1996).

[11] P. Mivelaz, J.-P. Jaccoud, R. Favre, Experimental study of air and water flow through cracked reinforced concrete tension members, in: 4th int. symp. on Utilization of High-strength/high performance concrete, Paris, 1996, pp. 1233–1242.

[12] D. Dauti, A. Tengattini, S. D. Pont, N. Toropovs, M. Briffaut, B. Weber, Analysis of moisture migration in concrete at high temperature through in-situ neutron tomography, Cement and Concrete Research 111 (2018) 41 – 55. doi:https://doi.org/10.1016/j.cemconres.2018.06.010. URL http://www.sciencedirect.com/science/article/pii/S0008884618301613

[13] M. Yehya, E. Andò, F. Dufour, A. Tengattini, Fluid-flow measurements in low permeability media with high pressure gradients using neutron imaging: Application to concrete, Nuclear Instruments and Methods in Physics Research Section A: Accelerators, Spectrometers, Detectors and Associated Equipment.

[14] A. Kaestner, M. Morgano, J. Hovind, E. Lehmann, Bimodal imaging using neutrons and x-rays, in: Proceedings of the International Symposium on Digital Industrial Radiology and Computed Tomography, http://www.ndt. net/events/DIR2015/Paper/58_Kaestner. pdf (last access: 19 August 2016), 2015.

[15] A. Kaestner, J. Hovind, P. Boillat, C. Muehlebach, C. Carminati, M. Z. E. Lehmann, Bimodal imaging at ICON using neutrons and X-rays, Physics Procedia 88 (2017) 314–321. doi:10.1016/j.phpro.2017.06.043.

[16] D. Mannes, F. Schmid, J. Frey, K. Schmidt-Ott, E. Lehmann, Combined neutron and x-ray imaging for non-invasive investigations of cultural heritage objects, Physics Procedia 69 (2015) 653–660.

[17] A. Tengattini, D. Atkins, B. Giroud, E. Andò, J. Beaucour, G. Viggiani, Next-grenoble, a novel facility for neutron and x-ray tomography in grenoble, in: Proc. 3rd International Conference on Tomography of Materials and Structures (Lund, Sweden, 26–30 June 2017), 2017.

[18] E. Tudisco, C. Jailin, A. Mendoza, A. Tengattini, E. Andò, S. A. Hall, G. Viggiani, F. Hild, S. Roux, An extension of digital volume correlation for multimodality image registration, Measurement Science and Technology 28 (9) (2017) 095401.
URL http://stacks.iop.org/0957-0233/28/i=9/a=095401

[19] B. D. Lucas, T. Kanade, An iterative image registration technique with an application to stereo vision, in: Proceedings of the International Joint Conference on Artificial Intelligence, Vancouver, BC, Canada, 1981, pp. pages 674–679.

[20] J. A. Bilmes, et al., A gentle tutorial of the em algorithm and its application to parameter estimation for gaussian mixture and hidden markov models, International Computer Science Institute 4 (510) (1998) 126.

[21] P. C. Mahalanobis, On the generalised distance in statistics, in: Proceedings National Institute of Science, India, Vol. 2, 1936, pp. 49–55.

[22] E. Andò, R. Cailletaud, E. Roubin, O. Stamati, the spam contributors, spam: The software for the practical analysis of materials, https://ttk.gricad-pages.univ-grenoble-alpes.fr/spam/ (2017–).

Appendix A. Registration algorithm

Appendix A.1. Multi-modal registration

It is reminded here that the goal of the registration algorithm is the find the best transformation $\boldsymbol{F}$ that deforms f_{n} to minimise $\mathcal{T}$. To do so an iterative approach is adopted which involves a progressive correction of an initial $\boldsymbol{F}$ by $\delta\boldsymbol{F}$. The correction at iteration $(n+1)$ is

$$\boldsymbol{F}^{(n+1)} = (\boldsymbol{I} + \delta\boldsymbol{F}^{(n+1)}) \cdot \boldsymbol{F}^{(n)} \tag{A.1}$$

The small quantity $\delta\boldsymbol{F}$ invites a first order Taylor expansion of $f_{\mathrm{n}}(\boldsymbol{F}^{(n+1)} \cdot \boldsymbol{x})$:

$$f_{\mathrm{n}}(\boldsymbol{F}^{(n+1)} \cdot \boldsymbol{x}) = f_{\mathrm{n}}(\boldsymbol{F}^{(n)} \cdot \boldsymbol{x}) + \nabla f_{\mathrm{n}}(\boldsymbol{F}^{(n)} \cdot \boldsymbol{x}) \cdot \delta\boldsymbol{F}^{(n+1)} \cdot \boldsymbol{F}^{(n)} \cdot \boldsymbol{x} \tag{A.2}$$

This equation is made more compact by introducing $\boldsymbol{x}^{(n)} = \boldsymbol{F}^{(n)} \cdot \boldsymbol{x}$, and the corrected image $\widetilde{f}_{\mathrm{n}}^{\,(n)}(\boldsymbol{x}) \equiv f_{\mathrm{n}}(\boldsymbol{x}^{(n)})$ with the current transformation so that

$$f_{\mathrm{n}}(\boldsymbol{F}^{(n+1)} \cdot \boldsymbol{x}) = \widetilde{f}_{\mathrm{n}}^{\,(n)}(\boldsymbol{x}) + \nabla \widetilde{f}_{\mathrm{n}}^{\,(n)}(\boldsymbol{x}) \cdot \delta\boldsymbol{F}^{(n+1)} \cdot \boldsymbol{x}^{(n)} \tag{A.3}$$

For the same reason, Φ^2 is expanded to the second order, with respect to the f_{n} above. This yields the functional:

$$\begin{aligned}\mathcal{T}\left(\boldsymbol{F}^{(n+1)}\right) = \sum_{\boldsymbol{x}\in\mathrm{ROI}} \Bigg[& \Phi^2(f_{\mathrm{x}}(\boldsymbol{x}), \widetilde{f}_{\mathrm{n}}^{\,(n)}(\boldsymbol{x})) \\ & + \frac{\partial\Phi^2(f_{\mathrm{x}}(\boldsymbol{x}), \widetilde{f}_{\mathrm{n}}^{\,(n)}(\boldsymbol{x}))}{\partial f_{\mathrm{n}}} \left(\nabla \widetilde{f}_{\mathrm{n}}^{\,(n)}(\boldsymbol{x}) \cdot \delta\boldsymbol{F}^{(n+1)} \cdot \boldsymbol{x}^{(n)}\right) \\ & + \frac{1}{2} \frac{\partial^2\Phi^2(f_{\mathrm{x}}(\boldsymbol{x}), \widetilde{f}_{\mathrm{n}}^{\,(n)}(\boldsymbol{x}))}{\partial f_{\mathrm{n}}^2} \left(\nabla \widetilde{f}_{\mathrm{n}}^{\,(n)}(\boldsymbol{x}) \cdot \delta\boldsymbol{F}^{(n+1)} \cdot \boldsymbol{x}^{(n)}\right)^2 \Bigg]\end{aligned} \tag{A.4}$$

The unknown is $\delta\boldsymbol{F}$. The minimum of the functional $\mathcal{T}$ (and not necessarily a zero) is looked for, and hence we solve for $\delta\boldsymbol{F}$ where its derivative is zero. The derivative of Equation A.4 yields:

$$\frac{d\mathcal{T}\left(\boldsymbol{F}^{(n+1)}\right)}{d\delta\boldsymbol{F}^{(n+1)}} = \sum_{\boldsymbol{x}\in\mathrm{ROI}}\left[\frac{\partial\Phi^2(f_\mathrm{x},\widetilde{f_\mathrm{n}}^{(n)})}{\partial f_\mathrm{n}} + \frac{\partial^2\Phi^2(f_\mathrm{x},\widetilde{f_\mathrm{n}}^{(n)})}{\partial f_\mathrm{n}^2}\left(\nabla\widetilde{f_\mathrm{n}}^{(n)}\cdot\delta\boldsymbol{F}^{(n+1)}\cdot\boldsymbol{x}^{(n)}\right)\right] \left(\nabla\widetilde{f_\mathrm{n}}^{(n)}(\boldsymbol{x})\otimes\boldsymbol{x}^{(n)}\right) \tag{A.5}$$

Solving for the zero-point of this derivative naturally leads to the following system

$$\boldsymbol{M}^{(n)}\delta\boldsymbol{F}^{(n+1)} = \boldsymbol{A}^{(n)} \tag{A.6}$$

where

$$\begin{cases} \boldsymbol{A}^{(n)} = -\sum_{\boldsymbol{x}\in\mathrm{ROI}}\frac{\partial\Phi^2(f_\mathrm{x},\widetilde{f_\mathrm{n}}^{(n)})}{\partial f_\mathrm{n}}\left(\nabla\widetilde{f_\mathrm{n}}^{(n)}\otimes\boldsymbol{x}^{(n)}\right) \\ \boldsymbol{M}^{(n)} = \sum_{\boldsymbol{x}\in\mathrm{ROI}}\frac{\partial^2\Phi^2(f_\mathrm{x},\widetilde{f_\mathrm{n}}^{(n)})}{\partial f_\mathrm{n}^2}\left(\nabla\widetilde{f_\mathrm{n}}^{(n)}\otimes\boldsymbol{x}^{(n)}\right)\otimes\left(\nabla\widetilde{f_\mathrm{n}}^{(n)}\otimes\boldsymbol{x}^{(n)}\right) \end{cases} \tag{A.7}$$

Equation A.6 is now developed for the potential function Φ^2 defined in the case of joint histogram fitted by bivariate Gaussian distributions. Deriving Φ^2 in Equation A.7 gives

$$\begin{cases} \frac{\partial\Phi^2(f_\mathrm{x},f_\mathrm{n})}{\partial f_\mathrm{n}} = b(f_\mathrm{x}-\mu_\mathrm{x}) + c(f_\mathrm{n}-\mu_\mathrm{n}) \\ \frac{\partial^2\Phi^2(f_\mathrm{x},f_\mathrm{n})}{\partial f_\mathrm{n}^2} = c \end{cases} \tag{A.8}$$

where $b, c, \mu_\mathrm{x}, \mu_\mathrm{n}$ are those associated with the phase selected by $\boldsymbol{\varphi}$ in the phase map (where each pixel is "labelled" with the most likely phase) and thus depend on each voxel position $\boldsymbol{x}$. In the interest of computational time, this composition map is computed in advance, and corrected when registration and phase fitting are estimated. This corresponds to a pre-calculation of what is presented in the voxel coverage maps in Figure 3. It is important to note that the voxel pairs falling into the non-phaseare simply excluded from the ROI.

Appendix A.2. Note on same-modality DVC

With images acquired with the same modality, the joint histogram will be essentially aligned along the $f_{\mathrm{x}} = f_{\mathrm{n}}$ diagonal line of $[p]$. This can be described as a single bivariate Gaussian distribution with parameters $a = 1$, $b = -1$ and $c = 1$, which aligns it along the diagonal. Inserted into Equation A.7, this yields the classical DVC operators $\boldsymbol{A}$ and $\boldsymbol{M}$ as obtained with the potential for same-modality DVC

$$\Phi^2(\boldsymbol{\varphi}) = \frac{1}{2}\left(f_{\mathrm{x}} - f_{\mathrm{n}}\right)^2 \tag{A.9}$$

This can be seen as a relaxation of classical DVC, and may present, for example a convenient way to take into account global changes of grey levels within the same modality.